Nanotechnology, Nanostructures, Nanomaterials

Initiated Chemical Vapor Deposition (iCVD) of Cross-linked Polymer Films for the Directed Self-assembly of Block Copolymers

P. Moni, K. K. Gleason
Sponsorship: NSF

Directed self-assembly (DSA) of block copolymer (BCP) thin films is a promising approach to enable next-generation patterning at increasingly smaller length scales. DSA uses a combination of physical and chemical constraints to force the BCP domains to self-assemble with the desired orientation with respect to the substrate. Physical constraints, such as holes and trenches, are formed using conventional lithographic techniques. Chemical constraints, or wetting layers, are thin films that are either sandwiched between the BCP film/substrate interface or coated on top of the BCP film. These wetting layers ensure the pattern formed upon self-assembly has the appropriate orientation with respect to the substrate. Controllable chemistry combined with facile processing is key to the integration of these wetting layers.

Here, we demonstrate that initiated chemical vapor deposited (iCVD) polydivinylbenzene (pDVB) ultra-thin films can direct the self-assembly of poly(styrene-block-methylmethacrylate) (PS-b-PMMA). iCVD allows for the simultaneous synthesis and formation of polymer thin films via a surface free radical polymerization.

Additionally, methyl radicals formed at increased filament temperatures can change the chemical structure of the growing pDVB film *in situ*. By tuning the degree of backbone methylation, we systematically changed the wetting properties of iCVD pDVB from weakly PMMA preferential to complete PS preference. Conformal coatings of weakly preferential iCVD pDVB films on topographical line and space patterns produced self-assembled BCP films with both perpendicular orientation and long-range alignment (Figure 1a and 1b). Current research efforts aim to use iCVD pDVB films to enable contact hole shrinkage. To minimize the diameter of the template hole, the BCP should assemble with a central, cylindrical PMMA domain. Preliminary experiments examined the effects of strongly PS-preferential, conformal iCVD pDVB films on a contact hole shrink template. The dark spot within each hole in Figure 1c corresponds to the PMMA domain. These results indicate that iCVD pDVB films are a viable method to enable contact-hole shrinkage.
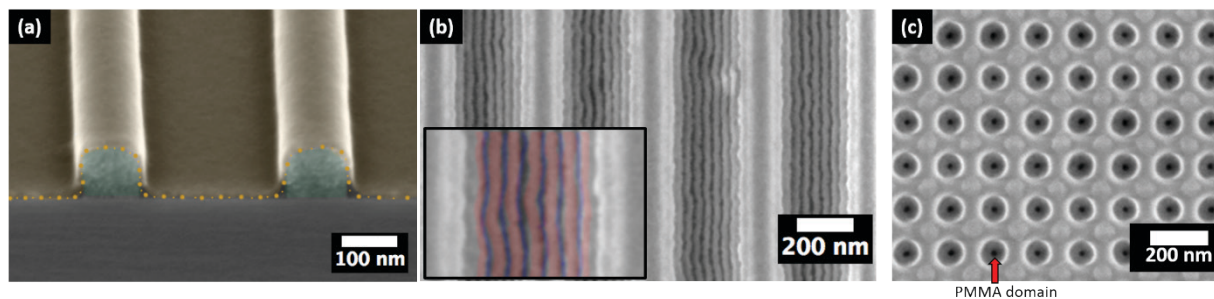
▲ Figure 1: (a) SEM image line and space template conformally coated with iCVD pDVB. Green highlight is trench template. Orange highlight is pDVB film. Orange dots highlight interface between pDVB film and template. (b) SEM image of self-assembled PS-b-PMMA inside line and space template coated with iCVD pDVB. Inset shows PS domains highlighted in red and PMMA domains highlighted in blue. (c) pDVB coated hole shrink template (ø = 65 nm) with self-assembled PS-b-PMMA inside holes. Red arrow indicates PMMA domain (central dark spot).

FURTHER READING

- P. Moni, H. S. Suh, M. Dolejsi, D. H. Kim, A. C. Mohr, P. Nealey, and K. K. Gleason, "Ultrathin and Conformal Initiated Chemical Vapor Deposited (iCVD) Layers of Systematically Varied Surface Energy for Controlling the Directed Self-assembly of Block co-Polymers," *Langmuir,* [in press], 2018.

Ising-Model-Based Computation by using Block Copolymer Self-assembly

H. Do, C. A. Ross, K. K. Berggren
Sponsorship: NSF, TSMC

Directed self-assembly of block copolymers can generate complex and well-ordered nanoscale patterns for lithography. Previously, self-consistent field theory has been commonly used to model and predict the block copolymer morphology resulting from a given template. In this work, we map block copolymer self-assembly onto an Ising model using two-dimensional post lattice template. We describe a simple and fast Ising-model-based simulation method for block copolymer self-assembly. With the Ising lattice setup, we demonstrate Ising-model-based logic gates.

Figure 1 shows a diagram of the Ising lattice setup. To define the Ising lattice, we used a post lattice template with horizontal and vertical pitch equal to the equilibrium block copolymer periodicity, L_0. After block copolymer processing, we defined a binary state, +1 or –1, between each adjacent pair of posts. We assigned +1 to a state when two adjacent posts were connected by a block copolymer structure, and –1 otherwise. The Ising Hamiltonian is given by

$$H(\sigma) = -J \sum_{\langle i\,j \rangle} \sigma_i \sigma_j - h \sum_j \sigma_j$$

where J's and h's were assumed to be independent of lattice location. We calculated the minimum Hamiltonian configuration using simulated annealing and compared the simulation results with previously reported results.

To perform Ising-model-based computation, we encoded Boolean operations into the ground states of Ising lattices by designing specific Hamiltonians. Figure 2 shows a template design for a buffer where a boundary was defined by incommensurate double posts. Inside the boundary, an input state and an output state were defined. Prior to block copolymer processing, the input state was determined by the

orientation of double posts while the output state was undetermined. After block self-assembly, the output state was set equal to the input state, performing the buffer operation.
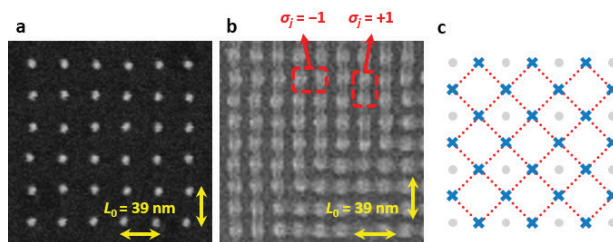
▲ Figure 1: (a) Square lattice post template fabricated by electron-beam lithography. (b) Block copolymer pattern formed on the post lattice template showing two degenerate alignment orientations. (c) A diagram showing the Ising lattice setup. The posts (grey dot), defined states (blue cross), and nearest-neighbor interactions (red dashed line) are indicated.
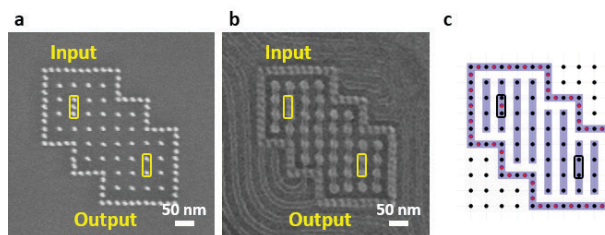
▲ Figure 2: (a) Template design for a buffer. An input state and an output state for the buffer are indicated. (b) After block copolymer processing, output state is set equal to the input state. (c) Minimum Hamiltonian configuration calculated from Ising-model-based simulation.

FURTHER READING

- J. Chang, H. Choi, A. F. Hannon, A. Alexander-Katz, C. A. Ross, and K. K. Berggren, "Design Rules for Self-assembled Block Copolymer Patterns using Tiled Templates," *Nature Communications*, vol. 5, no. 3305, pp. 1-9, Feb. 2014.

"Soft" Epitaxy in DNA-Nanoparticle Thin Films

P. A. Gabrys, R. J. Macfarlane
Sponsorship: NSF GRFP, AFOSR

The programmability of DNA makes it an attractive structure-directing ligand for the assembly of nanoparticle superlattices that mimic atomic crystallization. However, synthesizing multilayer single-crystals of defined size remains a challenge. This work studies growth temperature and interfacial energetics to achieve epitaxial growth of single crystalline nanoparticle thin films over arbitrarily shaped 500 × 500 μm² areas on lithographically patterned templates. Both surface morphology and internal structure are examined to provide an understanding of particle attachment and reorganization (Figure 1).

Importantly, these superlattices utilize a "soft," elastically malleable building block, resulting in significant strain tolerance when subjected to lattice mismatch.

Calculations of interaction potentials, small-angle X-ray scattering data, and electron microscopy images show that the oligomer corona surrounding a particle core can deform to store seven times more elastic strain than atomic films. DNA-nanoparticles dissipate strain both elastically through coherent relaxation of mismatched lattice parameter and plastically (irreversibly) through formation of dislocations or vacancies (Figure 2). Additionally, the DNA cannot be extended as readily as compressed, and thus, the thin films exhibit distinctly different relaxation behavior in the positive and negative mismatch regimes. These observations provide a more general understanding of utilizing rigid building blocks coated with soft compressible polymeric materials to control nano- and microstructure through "soft heteroepitaxy."
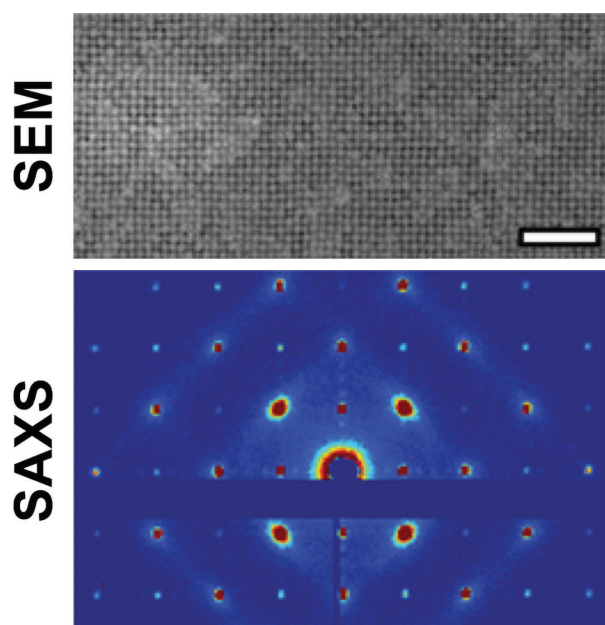
▲ Figure 1: Scanning electron microscopy (SEM) and small-angle X-ray scattering (SAXS) of a 10-layer DNA-nanoparticle thin film revealing near perfect, epitaxial alignment with the lithographically defined template. Scale bar is 500 nm.
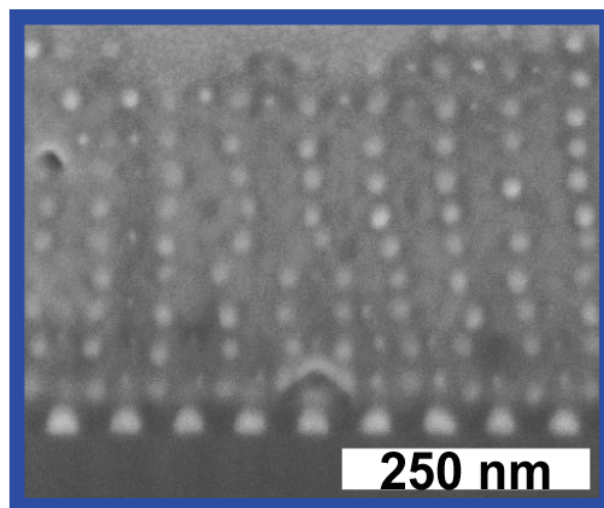
▲ Figure 2: SEM of cross-section following focused-ion-beam (FIB) milling of a DNA-nanoparticle thin film under negative lattice mismatch with respect to patterned lattice parameter exhibiting plastic strain dissipation through formation of a misfit dislocation.

FURTHER READING

- M. X. Wang, S. E. Seo, P. A. Gabrys, D. Fleischman, B. Lee, Y. Kim, H. A. Atwater, R. J. Macfarlane, and C. A. Mirkin, "Epitaxy: Programmable Atom Equivalents Versus Atoms," *ACS Nano,* vol. 11, no. 1, pp. 180-185, Jan. 2017.
- P. A. Gabrys, S. E. Seo, M. X. Wang, E. Oh, R. J. Macfarlane, and C. A. Mirkin, "Lattice Mismatch in Crystalline Nanoparticle Thin Films," *Nano Lett.,* vol. 18, no. 1, pp. 579-585, Jan. 2018.

Influence of TMAH Development on Niobium Nitride Thin Films

E. Toomey*, M. Colangelo*, N. Abedzadeh, K. K. Berggren
Sponsorship: IARPA
*equal author contribution

Patterning of superconducting thin films at the nanoscale has enabled numerous technologies used in signal detection and digital circuits. For instance, superconducting nanowire single photon detectors (SNSPDs) and, more recently, the nanocryotron (nTron) both make use of the ability to pattern niobium nitride films at dimensions < 100 nm. Electron beam lithography of these devices often employs the negative tone resist hydrogen silsesquioxane (HSQ) due to its high resolution and superior line edge roughness. Development of HSQ and adhesion promotion of HSQ to the substrate surface are both facilitated by tetramethylammonium hydroxide (TMAH), making it an integral chemical in the fabrication process. However, despite the prevalent use of TMAH in patterning superconducting films, its influence on the film itself has yet to be fully studied.

Here we have investigated the effects of exposing NbN thin films to 25% TMAH. We show that TMAH modifies the surface chemistry of the film by reacting with the NbN to form niobium-based clusters, which are visible by scanning electron micrograph inspection (Figure 1). In addition to thinning the overall NbN film and reducing its critical temperature, the formation of niobium clusters creates a barrier to reactive ion etching in CF_4, threatening the lithographic pattern transfer (Figure 2). While characterization such as FTIR has been employed to identify the compounds created by this reaction, future work is needed to study the mechanism through which the hexaniobate species interfere with the reactive ion etch chemistry.
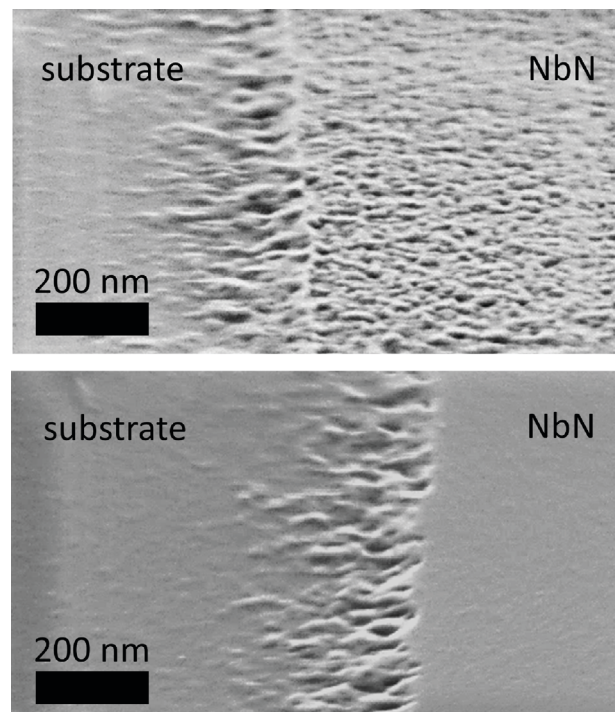
▲ Figure 1: Effect of TMAH on the surface of NbN. SEMs reveal the difference in surface features between an NbN structure that has been submerged in 25% TMAH (top) and one that has been untreated (bottom).
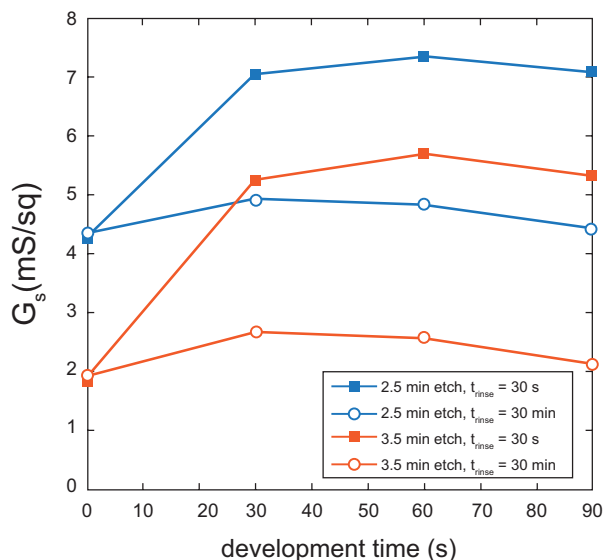
▲ Figure 2: *Impact of TMAH on the reactive ion etching of NbN*. Plot shows the sheet conductance versus development time in 25% TMAH. Conductances were measured after 2.5 min and 3.5 min of reactive ion etching (RIE) in CF_4. Samples were rinsed in DI water for either 30s (the standard process) or vigorously for 3 min. The data suggest that vigorous washing leads to roughly the same etch barrier thickness for each of the developed samples; however, the remaining NbN film thickness depends on the total time it has been developed. As a result, the resistance follows a directly proportional relationship with development time, since longer exposure to TMAH reduces the film thickness and increases the sheet resistance.

FURTHER READING

- L. B. Fullmer, R. H. Mansergh, L. N. Zakharov, D. A. Keszler, and M. Nyman, "Nb_2O_5 and Ta_2O_5 Thin Films from Polyoxometalate Precursors: A Single Proton Makes a Difference," *Cryst. Growth Des.*, vol. 15, no. 8, pp. 3885–3892, Aug. 2015.
- F. Najafi, A. Dane, F. Bellei, Q. Zhao, K. A. Sunter, A. N. McCaughan, and K. K. Berggren, "Fabrication Process Yielding Saturated Nanowire Single-photon Detectors with 24-ps Jitter," *IEEE J. Sel. Top. Quantum Electron*, vol. 21, no. 2, pp. 1–7, Mar. 2015.
- A. N. McCaughan and K. K. Berggren, "A Superconducting-nanowire Three-terminal Electrothermal Device," *Nano Lett.*, vol. 14, no. 10, pp. 5748–5753, Oct. 2014.

Empirical Modeling of Copper Semi-additive Electro-chemical Plating

C. I. Lang, D. S. Boning
Sponsorship: TSMC

Semi-additive electro-chemical plating (ECP) is a common process for fabricating copper interconnects in many advanced packaging technologies, such as Wafer Level Integrated Fan Out (InFO) packaging. While cost efficient, this process suffers from thickness variations in the height of the plated copper. The most significant of these variations are layout dependent, where areas with dense interconnects plate slower than sparse areas (Figure 1). If left unchecked, these variations can lead to significant complications in later stages of the fabrication process, and ultimately to decreased electrical performance of the final packaged device. Previously, there were limited methods for predicting these variations, and foundries had to rely on experimentally determining which layouts would perform acceptably. Recently, we have developed a model that predicts these variations and allows errors to be predicted and corrected without the need to first fabricate the layout in question.

While a model based on fundamental physics could in principle be developed to predict these variations, we instead develop an empirical model based on experimental data. This approach is well suited for many industrial applications, as empirical models can often be developed more quickly, without a significant loss of accuracy, and can be rapidly tuned or adapted to accommodate effects whose causes are uncertain. Our ECP model is divided into four stages as summarized in Figure 2. First, the effective pattern density of each point on the layout is determined with a learned spatial filter. These pattern densities are then mapped to effective conductances using a ratio-of-polynomials approximation. Next, these conductances are masked with the original layout, as photoresist prevents copper from growing in unwanted areas. Finally, the current flowing through each point of the wafer is solved for, and these currents are then converted to the plating height at each point in the layout.
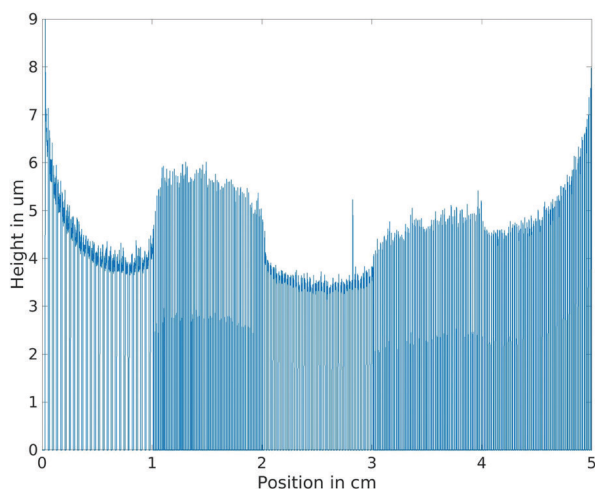
▲ Figure 1: Profilometry (height) scan across multiple regions of copper lines and spaces grown using ECP. Differences in the layout pattern density lead to different growth rates and structural variations.
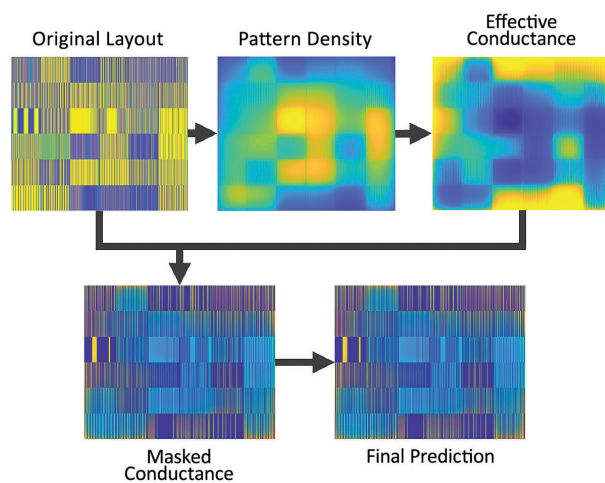
▲ Figure 2: Structure of the ECP model. Pattern densities are first determined and mapped to conductances. These are then used to solve for the currents, and finally for the plated height.

FURTHER READING

- C. I. Lang and D. S. Boning, "Modelling Pattern Dependent Variations in Semi-additive Copper Electrochemical Plating," *Advanced Semiconductor Manufacturing Conference (ASMC)*, 2018.

Additive Manufacturing of High-temperature Compatible Magnetic Actuators

A. P. Taylor, L. F. Velásquez-García
Sponsorship: Edwards Vacuum

Various MEMS devices require large displacement and large force actuation to be efficient, such as miniature pumps. Magnetic actuation delivers large displacement and large force in a compact form factor. Additive manufacturing has recently been explored as a processing toolbox for MEMS; researchers have reported additively manufactured microsystems with performance on par or better than counterparts made with standard microfabrication. In this work, miniature actuators are printed in pure Nylon 12 using the fused filament fabrication method where a thermoplastic filament is extruded from a hot nozzle to create layer by layer a solid object. The actuators have embedded magnets that are not demagnetized by the heated nozzle (@ 250 ˚C) while being sealed in place midstream in the printing process.

We have demonstrated the first miniature, additively manufactured, monolithic magnetic actuators compatible with high temperature (>200 ˚C) operation (Figure 1). The displacement of a 150 μm-thick, single-layer membrane actuator is characterized by various DC coil bias voltages, resulting in a maximum membrane displacement of 302 μm with 20V DC applied to the driving coil; in addition, the magnetic force is proportional to the square of the current drawn by the coil as expected from theory (Figure 2).
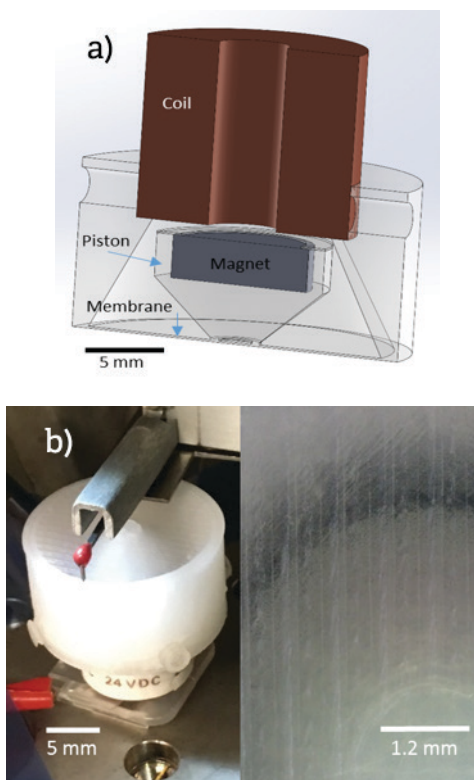
▲ Figure 1: (a) Cross-section of magnetic actuator with additively manufactured Nylon 12 body, embedded SmCo magnet, and off-the-shelf driving coil. (b) Photograph of a single-layer, 150 μm-thick membrane actuator while being tested (left) and close-up of the membrane showing the striations due to the rastering of the nozzle (right).
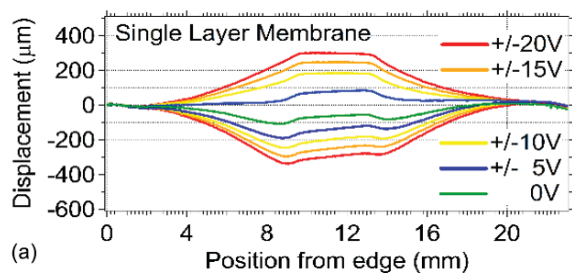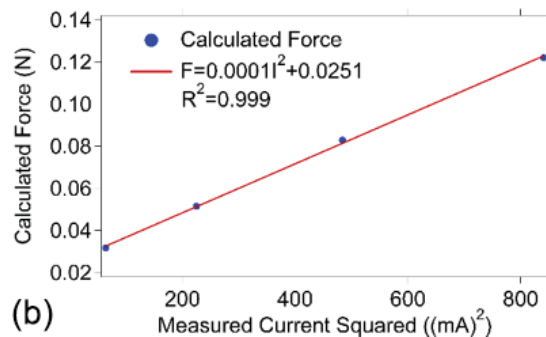
▲ Figure 2: (a) Membrane displacement vs. radial position from the edge for various DC bias coil voltages for an actuator with a 150 μm-thick single-layer membrane. The membrane sags at 0V due to the weight of the magnet. (b) Magnetic force acting on the SmCo magnet versus the square of the current drawn by the driving coil.

FURTHER READING

- A. P. Taylor and L. F. Velásquez–García, "High-temperature Compatible, Monolithic, -Printed Magnetic Actuators," *Proc. 17th PowerMEMS*, 2017.
- Z. Sun and L. F. Velásquez-García, "Monolithic FFF Printed, Biodegradable, Biocompatible, Dielectric–conductive Microsystems," J. *Microelectromech. Syst. 26*, vol. 6, pp. 1356–70, 2017.
- L. F. Velásquez-García, "SLA 3-D Printed Arrays of Miniaturized, Internally Fed, Polymer Electrospray Emitters," *J. Microelectromech. Syst. 24*, vol. 6, pp. 2117–27, 2015.

Electrospray-printed Physical Sensor

A. O. Sustaita-Narváez, L. F. Velásquez-García
Sponsorship: MIT-Tecnológico de Monterrey Nanotechnology Program

Electrospray deposition (ESD) has recently gained attention as a manufacturing technology to develop novel nanostructured composites to produce low-cost micro- and nano-devices. ESD is also a remarkably versatile printing technique due to its capability to create ultra-thin films made from a great variety of liquid feedstock (e.g., suspensions of polymeric, dielectric, metallic particles) that can be doped with organic nanostructures to modulate the physical properties of the imprint. Notably, the resulting nanoreinforced composites might show enhanced transduction, which, in combination with printing on flexible substrates, might be relevant for exciting applications such as wearable biomedical devices.

This project aims to develop an additively manufactured, low-cost, flexible physical sensor based on an ultrathin nanocomposite film doped with functionalized carbon nanostructures. The Taylor cone on an electrospray emitter fed with nanocomposite feedstock is shown in Figure 1a, while an electrospray-deposited imprint on a substrate is shown in Figure 1b. Essentially, this project is divided in *(i)* down-selecting and optimizing the formulation of the liquid feedstock, *(ii)* optimizing the fabrication of the ultrathin (~100 nm) nanostructured composite, and *(iii)* demonstrating a flexible physical sensor with transducing component made of the optimized nanostructured composite (see Figure 2).

▲ Figure 1: a) Taylor cone of nanocomposite solution (needle has 300 μm outer diameter). b) 150X scanning electron microscope image of a line of electrospray-deposited ultrathin nanocomposite film.
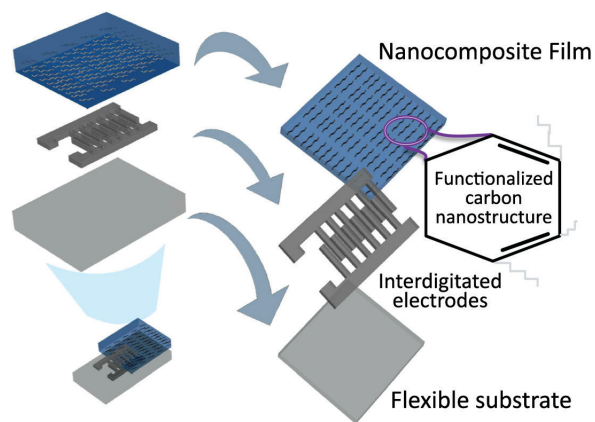
▲ Figure 2: Schematic of flexible physical sensor.

FURTHER READING

- D. Olvera-Trejo and L. F. Velásquez-García, "Additively Manufactured MEMS Multiplexed Coaxial Electrospray Sources for High-throughput, Uniform Generation of Core-shell Microparticles," *Lab Chip*, vol. 16, no. 21, pp. 4121-4132, 2016.
- A. P. Taylor and L. F. Velásquez-García, "Electrospray-printed Nanostructured Graphene Oxide Gas Sensors," *Nanotechnology*, vol. 26, pp. 505301:1-8, 2015.
- L. F. Velásquez-García, "SLA 3-D-Printed Arrays of Miniaturized, Internally-fed, Polymer Electrospray Emitters," *J. Microelectromechanical Systems*, vol. 24, no. 6, 2117-2127, 2015.

Atmospheric Microplasma Sputter Deposition of Interconnects

Y. Kornbluth, R. Mathews, L. Parameswaran, L. M. Racz, L. F. Velásquez-García
Sponsorship: MIT Lincoln Laboratory

We have preliminarily developed an apparatus that allows for the continuous, direct writing of interconnect-quality conductive lines. An atmospheric-pressure microplasma obviates the need for a vacuum while allowing for fine resolution imprints. We tested and characterized a novel focusing mechanism in which collisions with the working gas are harnessed to transfer electrostatic force to neutral sputtered atoms. This method compresses the deposit's width in one dimension while expanding its length in the perpendicular dimension. We find that for an ideal set of parameters, the imprint is narrower than the sacrificial sputtering target (i.e., 9 µm wide imprint from a 50 µm diameter target). Other sets of parameters lead to other results, as computer simulation predicted, ranging from an unfocused spot 400 µm in diameter to a narrow line with 20:1 compression in the direction of focus, i.e., width, and 20:1 expansion in length (Figure 1), as compared to the unfocused spot.

The microstructure of the deposit is of particular interest. As is typical of sputterers, the deposit could be smooth (55 nm roughness), and the resistivity can be as low as 1.1 µΩ·m (with no annealing). However, the resistivity greatly depends on the microstructure, which in turn depends on the deposition conditions. It is well known that sputtering at high-pressure results in a grain structure, as the early deposits shadow parts of the bare substrate, keeping sputtered material from fully coating the substrate. Traditionally, vacuum sputtering prevents this problem by allowing the sputtered material to impact the substrate normal to the surface; however, we sputter at atmospheric pressure, and thus, the sputtered material is redirected by random collisions. In our case, we use a combination of directed gas flow and electrostatic forces to prevent this shadowing effect (Figure 2).
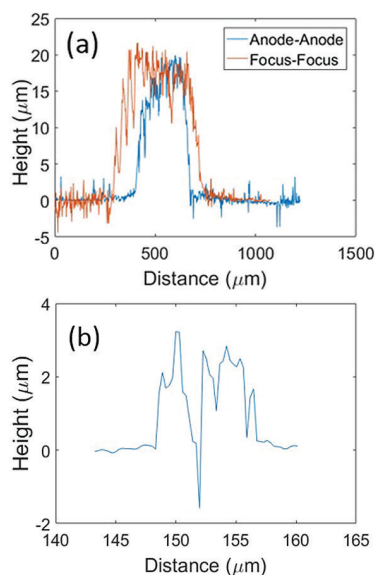
▲ Figure 1: Height profiles of (a) partially focused and (b) well-focused deposits. The well-focused deposit is cracked; an artifact of the microscopy extends the crack into the substrate.
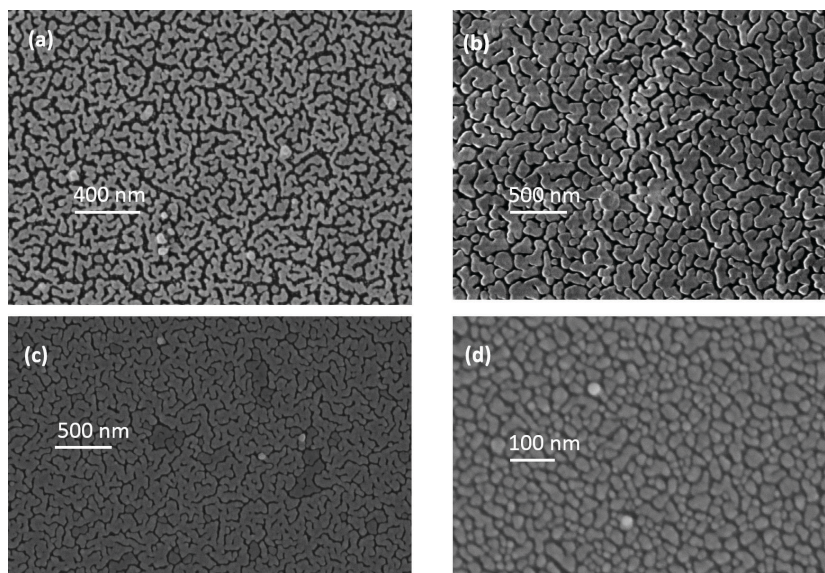
▲ Figure 2: SEM micrographs of deposits (a) without gas flow, (b) with gas flow but no electrostatic attraction, (c) with gas flow and electrostatic attraction, and (d) with gas flow and larger electrostatic attraction. Note how the microstructure improves from (a) to (c), and in (d), there is too much attraction for proper deposition.

FURTHER READING

- Y. Kornbluth, R. H. Mathews, L. Parameswaran, L. M. Racz, and L. F. Velásquez-García, "Microsputterer with Integrated Ion-drag Focusing for Additive Manufacturing of Thin, Narrow Conductive Lines," *J. of Physics D – Applied Physics*, vol. 51, no. 16, 165603, Apr. 2018.
- E. V. Heubel and L. F. Velásquez-García, "Microfabricated Retarding Potential Analyzers with Enforced Aperture Alignment for Improved Ion Energy Measurements in Plasmas," *J. of Microelectromechanical Systems*, vol. 24, no. 5, pp. 1355 - 1369, Oct. 2015.
- E. F. C. Chimamkpam, E. S. Field, A. I. Akinwande, and L. F. Velásquez-García, "Resilient Batch-fabricated Planar Arrays of Miniaturized Langmuir Probes for Real-time Measurement of Plasma Potential Fluctuations in the HF to Microwave Frequency Range," *J. of Microelectromechanical Systems,* vol. 23, no. 5, pp. 1131 – 1140, Oct. 2014.

Aligned CNT-based Microstructures and Nanoengineered Composite Macrostructures

B. L. Wardle, E. Cohen, H. Cornwell, N. Fritz, R. Kopp, J. Lee, R. Li, D. Lidston, X. Ni, I. Stein
Sponsorship: MIT NECST Consortium, NSF, AFRL, ARL, ONR, NASA NSTRT Fellowship, NDSEG Fellowship, NSF Fellowship

Materials comprising carbon nanotubes (CNTs), such as hierarchical nanoengineered advanced composites for aerospace applications, are promising new materials thanks to their mechanical and multifunctional properties. We have undertaken a significant experimentally based program to understand both microstructures of aligned-CNT nanocomposites and hierarchical nanoengineered advanced composites macrostructures hybridized with aligned CNTs.

Aligned nanocomposites are fabricated by mechanical densification and polymer wetting of aligned CNT forests. Here the polymer is typically an unmodified aerospace-grade epoxy. CNT forests are grown to mm-heights on 1-cm2 Si substrates using a modified chemical vapor deposition process. Following growth, the forests are released from the substrate and can be handled and infiltrated. The volume fraction of the as-grown CNT forests is about 1%; however, the distance between the CNTs (and thus, the volume fraction of the forest) can be varied by applying a compressive force along the two axes of the plane of the forest to give volume fractions of CNTs exceeding 20% (see Figure 1a). Variable-volume fraction-aligned CNT nanocomposites were characterized using optical, scanning electron (SEM), transmission electron (TEM) microscopy, 3-D TEM, and X-ray computed tomography (CT) to analyze dispersion and alignment of CNTs as well as overall morphology. Extensive mechanical property testing and modeling are underway, including 3-D constitutive relations and fracture toughness.

Nanoengineered hierarchical composites hybridized with aligned CNTs are prepared by placing long (>20 μm) aligned CNTs at the interface of advanced composite plies as reinforcement in the through-thickness axis of the laminate (see Figure 2). Three fabrication routes were developed: transplantation of CNT forests onto pre-impregnated plies ("nanostitching"), placement of detached CNT forests between two fabrics followed by subsequent infusion of matrix, and *in situ* growth of aligned CNTs onto the surface of ceramic fibers followed by infusion or hand-layup. Aligned CNTs are observed at the composite ply interfaces and give rise to significant improvement in interlaminar strength, toughness, and electrical properties. Extensions of the CNT-based architectures to ceramic-matrix nanocomposites and towards multifunctional capabilities are being developed, including structural health monitoring and deicing.
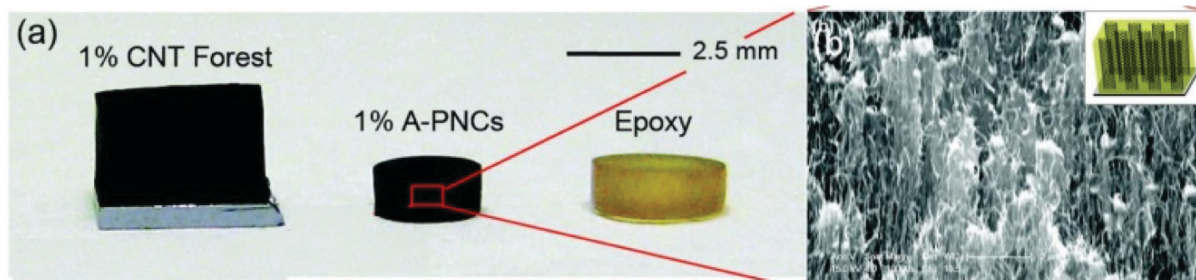
▲ Figure 1: Controlled-morphology polymer nanocomposites: (a) Image of 1% aligned-CNT forest, 1% A-PNCs and pure epoxy samples, (b) SEM image of 1% A-PNCs with an inset schematic of the CNT alignment direction.
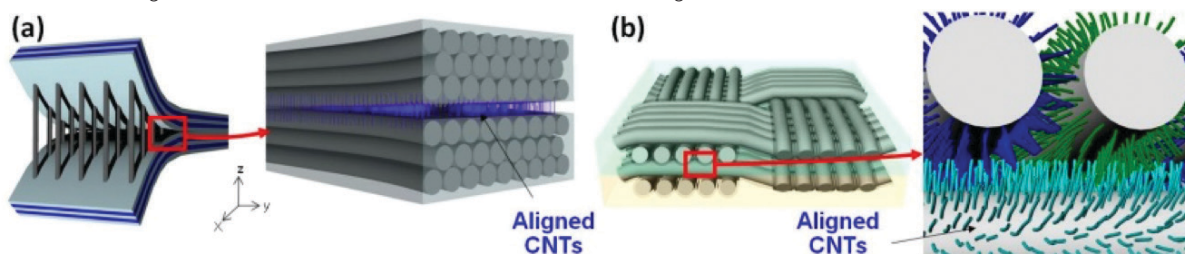
▲ Figure 2: Aligned-CNT nano-engineered composite macro-scale architectures, (a) nanostitching and (b) fuzzy fiber.

FURTHER READING

- L. Gorbatikh, B. L. Wardle, and S. V. Lomov, "Hierarchical Lightweight Materials for Structural Applications," *MRS Bulletin*, vol. 41, no. 9, 672-677, Sep. 2016.
- B. Natarajan, N. Lachman, T. Lam, D. Jacobs, B. L. Wardle, et al., "The Evolution of Carbon Nanotube Network Structure in Unidirectional Nanocomposites Resolved by Quantitative Electron Tomography," *ACS Nano*, vol. 9, no. 6, 6050-6058, 2015.

Geometry-dependent Properties of Synthetic Monolayer MoS$_2$

P. C. Shen, Y. Lin, J. Kong
Sponsorship: NSF E3S

Two-dimensional transition metal dichalcogenides (2-D TMDs) have shown great promise to be an ideal candidate for post-silicon technology. Their atomic thicknesses and large carrier effective masses can offer excellent electrostatic gate control, a reduced source-to-drain leakage current, and a higher on-current in the ballistic regime, potentially enabling ultra-scaled devices, tunnel field-effect transistors, and ballistic transistors. However, the intricacy and diversity of the structural defects in 2-D TMDs significantly affect their electrical and optical properties, in either beneficial or detrimental ways. In the case of monolayer MoS$_2$, several challenging issues including Femi level pinning at metal/MoS$_2$ interface, unintentional n-type doping, and carrier scatterings, non-radiative excitonic recombinations, etc., have been attributed to a considerable amount of sulfur vacancy in monolayer MoS$_2$.

On the other hand, specific types of defects, if controlled carefully, also offers the access to engineer the nature of monolayer MoS$_2$, such as channel polarity modification for realization of low-power MoS$_2$–based CMOS integrated circuits, exciton reservoirs to prolong the excitonic lifetime for high-performance optoelectronic and photonic devices.

This work explores the correlation between the domain geometries and the presence of different types of defects in monolayer MoS$_2$ synthesized by chemical vapor deposition through transport and spectroscopy measurements. We show that the shapes of MoS$_2$ domain can modulate the photoluminescence intensity and work function of MoS$_2$ monolayers and the threshold voltage in the MoS$_2$ field-effect transistors. Based on a two-defect-state model, the geometry-modulated behavior can be explained. This work not only offers a strategy to engineer the nature of MoS$_2$ from the synthesis perspective, but also pave a path to realize low-power MoS$_2$ CMOS integrated circuits.
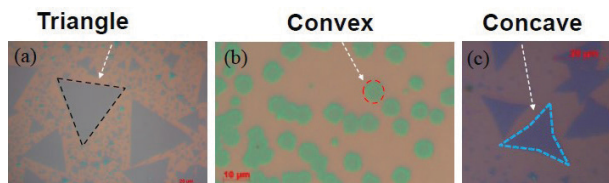
▲ Figure 1: Different domain shapes of CVD-grown MoS$_2$. Generally, they can be grouped into three geometries, namely, (a) triangle, (b) convex, and (c) concave.
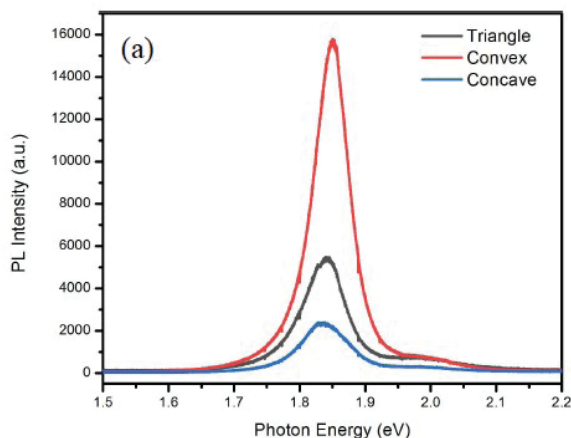
▲ Figure 2. Enhanced photoluminescence from convex MoS$_2$ monolayers. We infer that this PL enhancement originates from the presences of acceptor-like defect states near the valence band edge of the convex MoS$_2$.

FURTHER READING

- S. B. Desai, S. R. Madhvapathy, A. B. Sachid, J. P. Llinas, Q. Wang, G. H. Ahn, G. Pitner, M. J. Kim, J. Bokor, C. Hu, and H. S. P. Wong, "MoS2 Transistors with 1-Nanometer Gate Lengths," *Science*, vol. 354, no. 6308, pp. 99-102, 2016.
- S. Wang, Y. Rong, Y. Fan, M. Pacios, H. Bhaskaran, K. He, and J. H. Warner, "Shape Evolution of Monolayer MoS2 Crystals Grown by Chemical Vapor Deposition," *Chemistry of Materials*, vol. 26, no. 22, pp. 6371-6379, 2014.
- H. Qiu, T. Xu, Z. Wang, W. Ren, H. Nan, Z. Ni, Q. Chen, S. Yuan, F. Miao, F. Song, and G. Long, "Hopping Transport through Defect-induced Localized States in Molybdenum Disulphide," *Nature Communications*, vol. 4, pp. 2642, 2013.

Roll-to-Roll Transfer of Conductive Graphene Sheets

G. Azzellino, J. Kong
Sponsorship: MITEI, Eni SpA

Graphene technology has been widely explored to produce large sheets of conductive film to facilitate the manufacturing of flexible transparent photovoltaics. Monolayer-thick graphene has 97% transmittance in the visible regime and outstanding mechanical and electrical properties: that makes graphene suitable for transparent electrodes in order to replace the current state-of-the-art ITO electrodes, which are less flexible and are limited by the low indium supply on earth. However, scaling up the graphene manufacturing is tricky since it is typically grown on copper foils by chemical vapor deposition (CVD), and therefore, an additional transfer step is required to insert the graphene sheet into practical devices. The success of the transfer process is critical for the performances and the scalability of the graphene film.

Given the compatibility with the manufacturing processes in organic and flexible electronics, we explore roll-to-roll (R2R) to enable the deployment of large area graphene on plastic substrates. We investigate how to avoid defects and fractures in the graphene film upon transfer. We scan over several options in order to figure out how the interplay of adhesion forces between the graphene and the host substrate works out. These investigations will advance the progress of the application of graphene in future flexible electronics.

FURTHER READING:

- M. Hempel, A.-Y. Lu, F. Hui, T. Kpulun, M. Lanza, G. Harris, T. Palacios, and J. Kong "Repeated Roll-to-Roll Transfer of Two-dimensional Materials by Electrochemical Delamination," *Nanoscale 12,* 2018.

150 °C Copper Bonding Technology with Graphene Interlayer

H. Wang, W. S. Leong, F. Hu, L. Ju, C. Su, Y. Guo, J. Li, M. Li, A. Hu, J. Kong
Sponsorship: NSF

Bonding technology plays a significant role in electronic packaging as it provides physical and electrical connections between semiconductor chips. Reliability of bonding joints affects the energy consumption and speed of an electronic system. Hence, it is important to have a reliable bonding technology. Copper (Cu) bonding technology is one of the most frequently-used bonding technologies nowadays. However, two critical issues have been limiting the reliability of lead-free Cu bonding technology: high bonding temperature (~260 °C) and aging degradation.

We have devised a graphene-based Cu bonding technology that is of low bonding temperature and high reliability. By integrating nanoscale graphene/Cu composite on the Cu substrate prior to thermocompression bonding, Sn-Cu joints can be fabricated at a bonding temperature as low as 150 °C, which is the lowest reported value to date for Cu bonding technology. Specifically, we electrochemically deposit a layer of Cu nanocone array on the Cu substrate and cover it with a graphene sheet, prior to the bonding process. When subjected to heat, microscale Sn solder deforms and replicates the Cu nanocone array morphology, and hence transforming into nanoscale Sn. Compared to microscale Sn, nanoscale Sn has much lower melting points and facile surface diffusion. This phenomenon effectively contributes to the low bonding temperature observed in our bonding technology. The presence of the graphene layer prevents the formation of Cu-Sn intermetallic compounds thus significantly slows down the aging degradation. With the advancement in graphene synthesis and transfer technology, we anticipate the graphene-based Cu bonding technology presented in this work can be integrated into the existing commercial Cu bonding technology for industrial applications in the near foreseeable future.
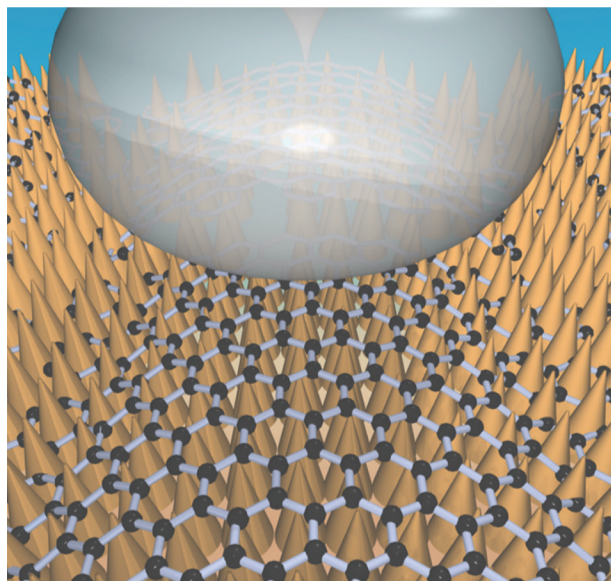
▲ Figure 1: Schematic illustration of our graphene-based copper bonding technology.
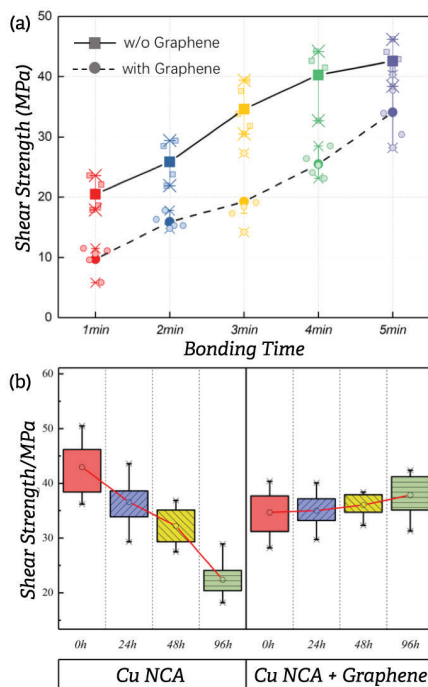
▲ Figure 2: (a) Shear strength distribution of both the Sn−Cu and Sn−graphene−Cu bonds as a function of bonding duration. (b) Shear strength distribution of the Sn−Cu (left) Sn-graphene-Cu (right) bonds as a function of aging duration.

FURTHER READING

- H. Wang, W. S. Leong, F. Hu, L. Ju, C. Su, Y. Guo, J. Li, M. Li, A. Hu, and J. Kong, "Low-temperature Copper Bonding Strategy with Graphene Interlayer," *ACS Nano,* vol. 12, no. 3, pp. 2395–2402, 2018.

Chemical Vapor Deposition of Multiple Transition Metal Disulfides in One Synthesis Step

W. S. Leong, J. Kong
Sponsorship: MIT-SUTD Postdoctoral Fellowship, AFOSR FATE-MURI

Recently, transition metal disulfides (TMD) have received tremendous attention due to their exceptional optical and electrical properties. Many techniques have been explored to obtain monolayer TMD and chemical vapor deposition (CVD) synthesis using transition metal oxide, and chalcogenide solid precursors is the most common method used in laboratories now. However, the quantity of solid precursors used is usually surplus giving rise to chemical reactions between precursors in each of their crucibles, as a result of precursors' diffusion at growth temperature. Hence, a CVD setup is normally dedicated for the growth of only one type of TMD to avoid cross-contamination (except for hetero-structures synthesis), and it is impossible to grow multiple monolayer TMD in one synthesis step. Here, we report a new technique to synthesize MoS_2 and WS_2 monolayer films in one CVD process. We first disperse a minuscule amount of metal oxide precursor on targeted substrates, which were then loaded to the furnace in slanting position, rather than horizontal, followed by a sulfur annealing to concurrently grow monolayer MoS_2 and WS_2 on separate substrates. The synthesized TMD films exhibit good properties as confirmed by Raman, PL, XPS, STEM analyses, and electrical measurements.
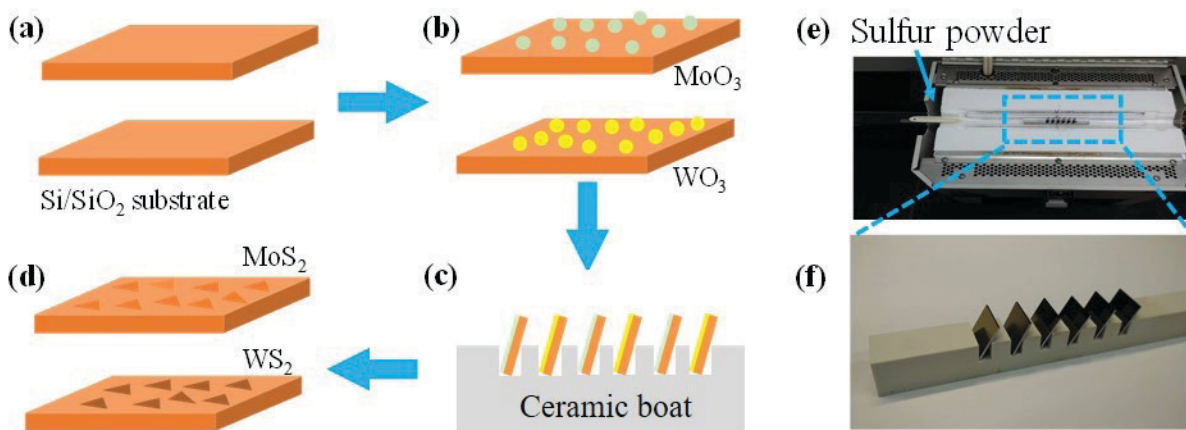
▲ Figure 1: a-d) Schematic illustration of the concurrent synthesis process of monolayer MoS_2 and WS_2. e) Image showing experimental setup used. f) Image showing the custom-made ceramic boat which was designed such that multiple Si/SiO_2 wafers can be loaded at once in slanting position.

FURTHER READING

- W. S. Leong, L. Sun, S. Yang, M. F. Chisholm, S.-J. Liang, L. K. Ang, Y. Tang, Y. Mao, H. Y. Yang, and J. Kong, "Concurrent Synthesis of High-performance Monolayer Transition Metal Disulfides," *Advanced Functional Materials,* vol. 27, pp. 1605896, 2017.

Remote Epitaxy through Graphene for Two-dimensional Material Based Layer Transfer

Y. Kim, K. Lee, K. Qiao, S. Bae, H. Kum, W. Kong, J. Kim
Sponsorship: Masdar Institute, LG Electronics, DARPA, AFRL

Van der Waals epitaxy (vdWE) has gained great interest for crystalline growth as it substantially relaxes the strict lattice matching requirements in conventional heteroepitaxy and allows for facile layer release from the vdWE surface. In recent studies, vdWE was investigated on two-dimensional (2-D) materials grown or transferred on arbitrary substrates, with the primary notion that the 2-D material is the sole epitaxial seed layer in vdWE. However, the underlying substrate may still play a role in determining the orientation of the overlayers since the weak vdW potential field from 2-D materials may barely screen the stronger potential field from the substrates.

Here, we reveal that the epitaxial registry of adatoms during epitaxy can be assigned by the underlying substrate remotely through 2-D materials by modulating the interaction gap between the substrate and the epilayer. Our study shows that remote epitaxial growth can be performed through a single-atom-thick gap defined by monolayer graphene at the substrate-epilayer interface. Simulations using density functional theory (DFT) prove that remote epitaxy can occur within a ~9 Å substrate-epilayer gap. We experimentally demonstrate successful remote homoepitaxy of GaAs(001) on GaAs(001) substrates through monolayer graphene (Figure 1). Characterization by high-resolution scanning transmission electron microscopy (HRSTEM) confirms single crystalline growth of GaAs film through graphene with an interaction gap of 5 Å below the critical limit outlined by the simulation. The concept of remote homoepitaxial growth is further extended to other compound semiconductors such as InP, GaP, GaN, as well as functional oxides, $SrTiO_3$, and fluoride material systems, LiF (Figure 2). Following the growth, the single-crystalline films are rapidly released from the vdW surface of graphene to provide large-scale, single-crystalline films. This concept, here termed 2-D material based layer transfer (2-DLT), suggests a universal method to copy/paste epitaxial films of any material systems based on the underlying substrates through 2-D materials then rapidly release and transfer to substrates of interest. The potential to reuse graphene-coated substrates suggests 2-DLT will greatly advance non-Si electronics and photonics by displacing the high cost of non-Si substrates.
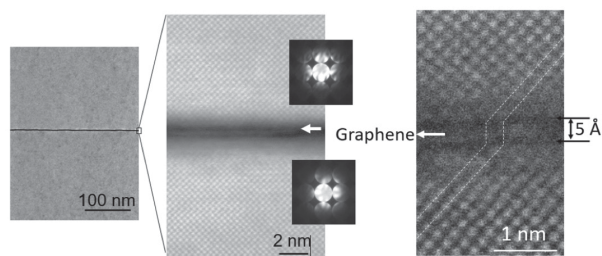
▲ Figure 1: High-resolution STEM images showing excellent remote alignment of the (001) GaAs lattices through the graphene. Convergent beam electron diffraction patterns (001) from the epilayer (top) and the substrate (bottom) show identical zinc blend (001) orientations.
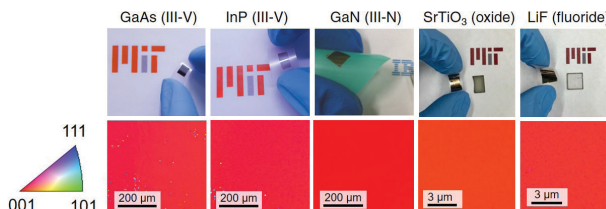
▲ Figure 2: EBSD mapping of exfoliated films grown via remote epitaxy demonstrating large-scale single-crystalline growth of III-V, III-N, oxide, and fluoride materials. The inverse pole figure color triangle (left) indicates (001) single-crystallinity of exfoliated films.

FURTHER READING

- Y. Kim, S. Cruz, K. Lee, B. O. Alawode, C. Choi, Y. Song, J. M. Johnson, J. Kim, et al., "Remote Epitaxy through Graphene for Two-dimensional Material Based Layer Transfer," *Nature*, vol. 544, no. 7650, pp. 340-343, 2017.

Towards Dislocation-free GaN

W. Kong, K. Qiao, J. Kim
Sponsorship: Analog Devices, Inc.

The performance of advanced GaN-based electronics and optoelectronics can rely heavily on the structural quality of the epilayer used in its fabrication. The layer's characteristics, such as dislocation density or surface roughness, are largely inherited from the initial GaN growth. Due to the limited availability and the cost of high-quality bulk GaN substrates, heteroepitaxy of GaN on foreign substrates such as Al_2O_3, SiC, and Si is conventionally used. The lattice and thermal-expansion-coefficient mismatch of these substrates to GaN unavoidably lead to the formation of dislocations, as well as potential cracks and wafer bow.

In addition, the majority of the substrate material is usually removed from state-of-the-art devices to lower the thermal resistance of the packaged devices and improve performance. The removal of GaN devices from bulk/foreign substrates is very challenging and is an ongoing subject of research. Existing removal processes involving photoelectrochemical etching, mechanical spalling, and laser interface decomposition suffer from slow processing speed and/or significant surface roughening and cracking, limiting the process yield and practicality of substrate reusing.

Recently, we discovered that the epitaxial registry of adatoms could be determined by the underlying substrate remotely without direct contact with the substrate, but through a narrow gap defined by monolayer graphene. Therefore, homoepitaxial growth can be performed remotely through the single-atom-thickness gap, with the dislocation density of the epitaxial thin film at the same level as the high-quality substrate. In addition, because of the van der Waals interaction at the graphene interface, the epitaxial thin film can be precisely and rapidly exfoliated from the substrate, demonstrating the atomic flatness at the released surface mimicking the morphology of graphene surface. We performed the remote epitaxy of GaN on GaN/sapphire substrate with monolayer graphene as an interlayer to demonstrate high-quality, low dislocation density GaN thin films. We obtained GaN epilayer with material quality identical to the GaN/sapphire substrate in terms of surface morphology and dislocation density. We further exfoliated the GaN epitaxial thin film from the substrate achieving free-standing GaN of 300nm thick.

Ultimately, we will develop the process of GaN remote epitaxy on bulk GaN substrate with minimal defects, enabling the GaN-based electrical and optoelectronic devices approaching intrinsic performance without the limitation from material quality. On the other hand, the cost of such high-performance devices will be significantly reduced since expensive substrates will be reused.
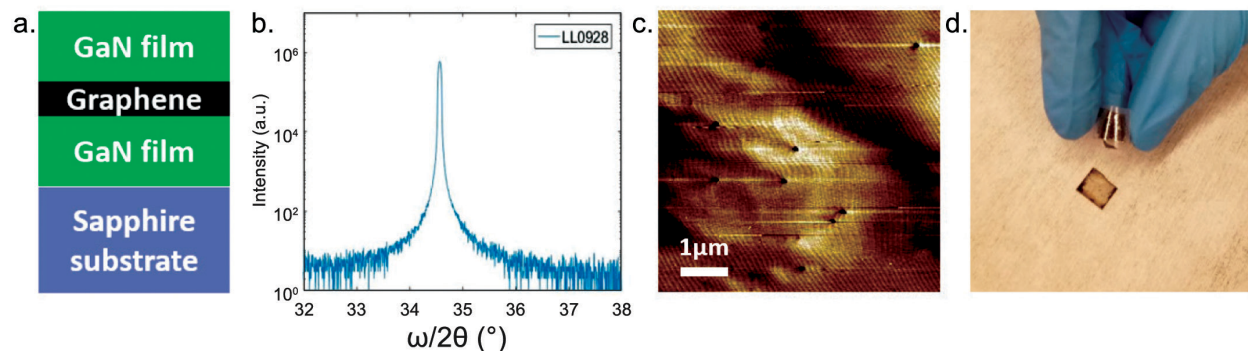
▲ Figure 1. a. Schematic diagram of remote epitaxy of GaN on GaN/sapphire template. b. High resolution X-ray diffraction ω/2θ scan of GaN showing (0002) peak. c. Surface morphology of remote epitaxial GaN. d. Exfoliation of thin film remote epitaxial GaN.

Electro-Chemo-Mechanical Studies of Perovskite-Structured Mixed Ionic-electronic Conducting $SrSn_{1-x}Fe_xO_{3-x/2+\delta}$

C. S. Kim, S. R. Bishop, N. H. Perry, H. L. Tuller
Sponsorship: Skolkovo Foundation

High efficiency and fuel flexibility make solid oxide fuel cells (SOFCs) attractive for conversion of fuels to electricity. Reduced operating temperatures, desirable for reduced costs and extended operation, however, result in significant losses in efficiency. This loss has been traced primarily to slow cathode surface reaction kinetics. In this work, we extend previous studies on the promising mixed ionic and electronic conducting perovskite-structured $SrTi_{1-x}Fe_xO_{3-x/2+\delta}$ (STF) materials system whose exchange kinetics were correlated with the minority electron charge density by replacing Ti with Sn, due to its distinct band structure and higher electron mobility.

Oxygen nonstoichiometry and the defect chemistry of the $SrSn_{1-x}Fe_xO_{3-x/2+\delta}$ (SSF) system were examined by thermogravimetry as a function of oxygen partial pressure in the temperature range of 973-1273 K. Marginally higher reducibility was observed compared to corresponding compositions in the STF system. The bulk electrical conductivity was measured in parallel to examine how changes in defect chemistry and electronic band structure, associated with the substitution of Ti by Sn, impact carrier density and ultimately electrode performance. Bulk chemical expansion was measured by dilatometry as a function of oxygen partial pressure, while surface kinetics were examined using AC impedance spectroscopy. The electrochemical properties of SSF were found not to differ significantly from the corresponding composition in STF. Though slightly shifted by the larger size of Sn, the defect equilibria and the cathode area specific resistance differed only in a limited way from that in STF. This was attributed to properties being largely dominated by Fe and not by the substitution of Ti with Sn. However, due to asymmetry in the crystal structure caused by the larger size of Sn, both thermal and chemical expansion coefficients of SSF35 were found to be around 20% and 10% lower than those of STF35, thus making SSF35 much more chemo-mechanically stable in SOFC operating conditions.
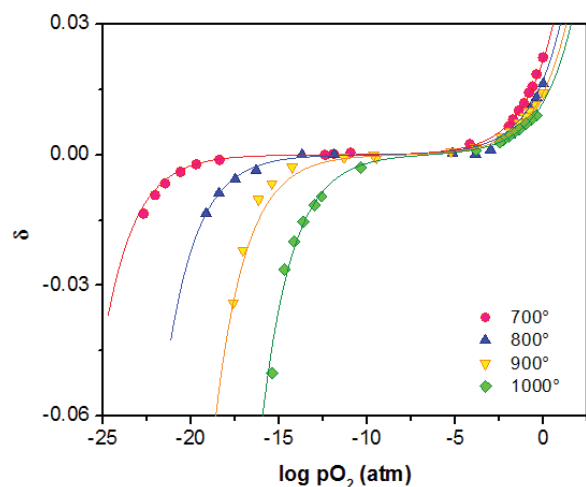
▲ Figure 1: Oxygen nonstoichiometry δ as a function of pO_2 and temperature for SSF35.
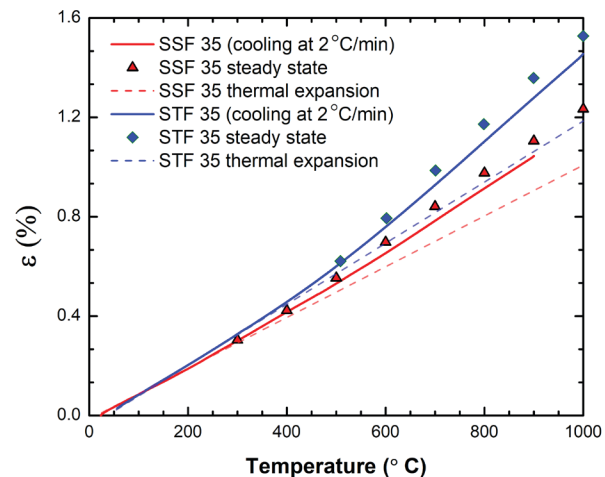
▲ Figure 2: Measured strains (solid lines), thermal expansions extended from low-temperature regimes (dashed lines) and steady-state strains (points) of SSF35 (red) and STF35 (blue).

FURTHER READING

- C. S. Kim, S. R. Bishop, and H. L. Tuller, "Electro-Chemo-Mechanical Studies of Perovskite-structured Mixed Ionic-electronic Conducting $SrSn_{1-x}Fe_xO_{3-x/2+\delta}$ Part II: Electrical Conductivity and Cathode Performance," *J. Electroceram.*, vol. 40, pp. 57-64, 2018.
- C. S. Kim, N. H. Perry, S. R. Bishop, and H. L. Tuller, "Electro-Chemo-Mechanical Studies of Perovskite-structured Mixed Ionic-electronic Conducting $SrSn_{1-x}Fe_xO_{3-x/2+\delta}$ Part III: Thermal and Chemical Expansion," *J. Electroceram.*, 2018.
- C. S. Kim, S. R. Bishop, and H. L. Tuller, "Electro-Chemo-Mechanical Studies of Perovskite-structured Mixed Ionic-electronic Conducting $SrSn_{1-x}Fe_xO_{3-x/2+\delta}$ Part I: Defect Chemistry," *J. Electroceram.*, vol. 38, pp. 74-80, 2017.

Controlling Concentration and Nature of Oxygen Defects in Layered Cuprate-based Materials by Electrical Bias

C. S. Kim, H. L. Tuller
Sponsor: Skolkovo Foundation

Both the nature and concentration of oxygen defects in oxide materials can have a significant impact on their physical and chemical properties, as well as key interfacial reaction kinetics such as oxygen exchange with the atmosphere. Most commonly, the desired oxygen defect concentration, or equivalently oxygen nonstoichiometry, is attained in a given material by controlling the oxygen partial pressure and temperature in which it is equilibrated or annealed. This approach, however, is limited by the range of oxygen partial pressures readily experimentally achievable and requires knowledge of the applicable defect chemical model.

In this study, we fine-tune oxygen defect concentrations in promising rare earth cuprate (RE_2CuO_4: RE = rare earth) solid oxide fuel cell (SOFC) cathode materials by application of electrical potentials across a yttria-stabilized zirconia (YSZ) supporting electrolyte. These layered perovskites can incorporate both oxygen interstitials and vacancies, thereby broadening the range of investigations. Here, we show a strong correlation between oxygen nonstoichiometry values (which are determined by *in situ* measurement of chemical capacitance) and oxygen surface exchange kinetics (which is inversely proportional to the area-specific-resistance). Both types of oxygen defects – interstitials and vacancies – dramatically enhance surface kinetics. These studies are expected to provide further insight into the defect and transport mechanisms that support enhanced SOFC cathode performance.
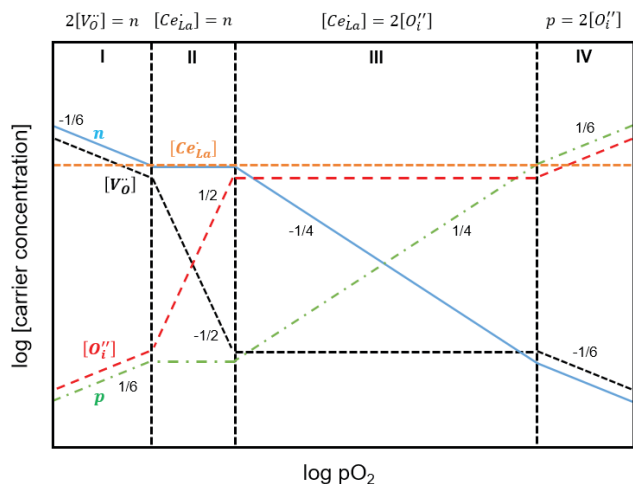
▲ Figure 1: Schematic defect diagram using Brouwer approximation for $La_{1.85}Ce_{0.15}CuO_{4+\delta}$ (LCCO).
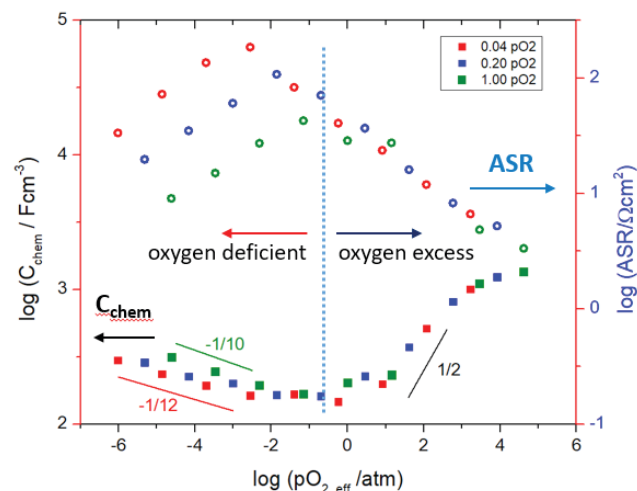
▲ Figure 2: Volumetric chemical capacitance (C_{chem}, closed squares) and area-specific-resistance (ASR, open circles) of LCCO thin film as functions of effective oxygen partial pressure at 600 °C in log-log plots. Three colors represent three different atmospheres (1.00 atm, 0.20 atm, and 0.04 atm oxygen partial pressures).

FURTHER READING

- C. S. Kim and H. L. Tuller, "Fine-tuning of Oxygen Vacancy and Interstitial Concentrations in $La_{1.85}Ce_{0.15}CuO_{4+\delta}$ by Electrical Bias," *Solid State Ionics*, vol. 320, pp. 233-238, Jul. 2018.
- D. Chen and H. L. Tuller, "Voltage-controlled Nonstoichiometry in Oxide Thin Films: $Pr_{0.1}Ce_{0.9}O_{2-\delta}$ Case Study," *Advanced Functional Materials*, vol. 24, issue 48, pp. 7638-7644, Dec. 2014.

Coherent Soft X-ray Imaging of Magnetic Nanotextures

J. Li, J. Pelliciari, R. Comin
Sponsorship: MIT Startup Funds, NSF

The ability to image the nanoscale structure of materials with tunable magnetic textures is pivotal for the development of low-power and nonvolatile data storage technologies. Soft X-ray imaging has emerged in the last decade as a powerful and accurate methodology to resolve the bulk domain structure of several magnetic materials — magnetic multilayers, buried interfaces, or skyrmion lattices — as well as nanoelectronic devices under operating conditions.

Soft X-ray imaging relies on two main requirements: (i) the ability to focus a collimated X-ray beam on a spot the size of a few tens of nm and (ii) the ability to scan the focused X-ray beam with nm precision. We have commissioned a new soft X-ray nanofocusing setup installed at beamline CSX-1 of the National Synchrotron Light Source II. The schematics of this setup are shown in Figure 1. A key element is the Fresnel zone plate (inset D), which acts as a diffractive phase mask to focus X-rays to a 70-nm spot at the sample, and is fabricated using e-beam lithographic tools. The beam spot can be moved with the aid of piezo-based nanopositioners (inset C), which translate the X-ray optics while keeping the sample in a fixed position. Diffracted X-rays are collected with a CCD camera in the far field (~30 cm from the sample). The resulting magnetic scattering intensity encodes local antiferromagnetic strength and can be acquired in less than a second. By scanning the X-ray beam across the sample, we are able to probe the spatial distribution of antiferromagnetic order.

We applied this new method to the study of antiferromagnetic rare earth $NdNiO_3$. In particular, and for the first time, we unveil the inhomogeneous nature of the spin-ordered ground state (inset B). Furthermore, we identify the spatial distribution of antiferromagnetic domains and show that it follows a scale-free distribution. Our future focus is to extend our studies to the imaging of nanoscale magnetic textures in antiferromagnetic spintronic materials and devices, including in operando studies as a function of applied current.
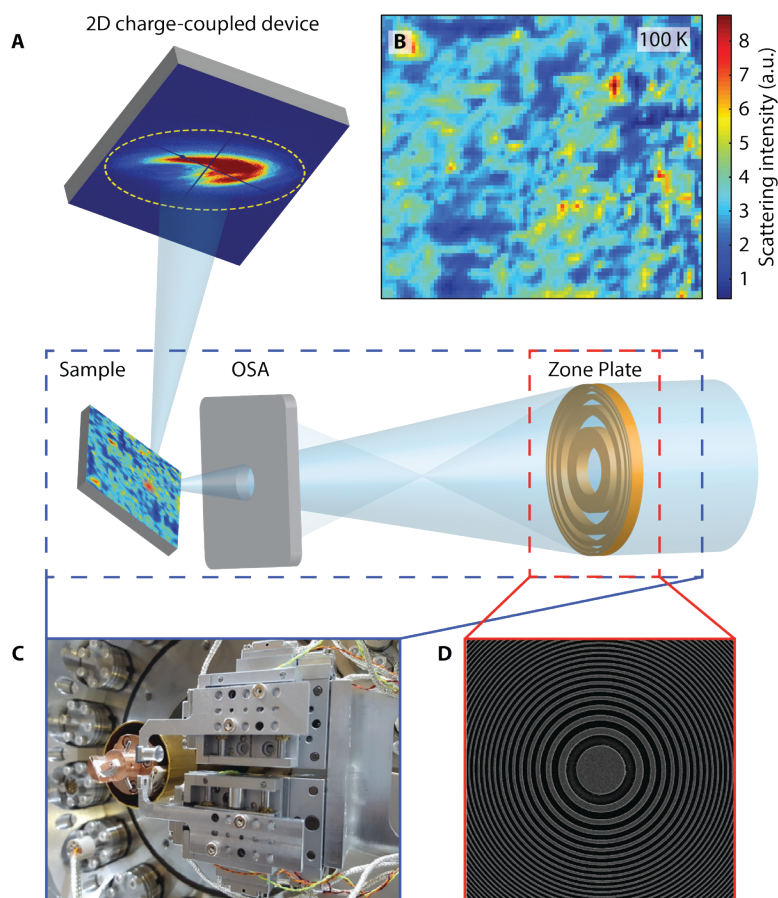
Figure 1: Resonant soft X-ray scattering nanoprobe setup at the National Synchrotron Light Source II. A. schematics of the X-ray optics used in the experiment; a Fresnel zone plate (fabricated at MTL; SEM image in D) focuses X-rays down to a ~70-nm spot at the sample position; diffracted X-rays are imaged with a CCD camera. B. inhomogeneous distribution of antiferromagnetic domains. C. inside view of the diffraction chamber, with piezo-actuated nanopositioners located upstream of the sample stage (copper). D. SEM image of the center of a Fresnel zone plate fabricated at MTL.

Fabrication of Small-pitch Gratings for Smith-Purcell Radiation from Low-energy Electrons

Y. Yang, A. Massuda, C. Roques-Carmes, S. E. Kooi, Y. Yang, C. Murdia, I. Kaminer, M. Soljačić, K. K. Berggren
Sponsorship: ARO, NSF

Swift-moving electrons carry evanescent near-field, which can be coupled to far-field radiation when the electrons move closer to a periodic structure and in parallel to the periodic structure plane. This effect was named after Smith and Purcell, following their first experimental demonstration of the effect. The wavelength of Smith-Purcell radiation depends on the grating pitch and the electron energy. Here, we demonstrate Smith-Purcell radiation in the optical regime by using gratings with 50-60 nm pitch and electrons with 1.5-6 keV kinetic energy. These results have potential applications in tunable nanoscale light sources.

Our gratings were fabricated on gold-coated silicon substrates. The 200-nm-thick gold coating layer was used to suppress cathodoluminescence from silicon. The grating patterns were defined using electron beam lithography in PMMA resist, followed by 0 ˚C cold development in 3:1 IPA:MIBK. 20 nm gold was then deposited via electron-beam evaporation and lifted-off in hot NMP. Figure 1 shows an SEM image of a 50-nm-pitch grating.

To measure Smith-Purcell radiation, the grating samples were mounted inside a modified SEM with an optical attachment to collect the radiated light and measure its spectrum. Electrons with 1.5-6 keV kinetic energy were used to induce the Smith-Purcell radiation. Figure 2 shows the measured Smith-Purcell radiation spectra from a 50-nm-pitch grating using electron beams with different kinetic energies. The peaks of the radiation spectra match well with the theoretical predictions (vertical dashed lines). We demonstrate the Smith-Purcell radiation wavelength decreases as we increase the electron kinetic energy or decrease the grating pitch.
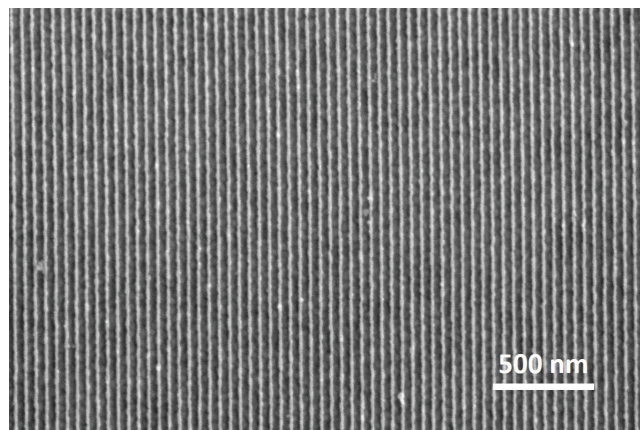
▲ Figure 1: Gold gratings with 50 nm pitch. The grating lines were fabricated on top of a silicon substrate coated with 200 nm gold.
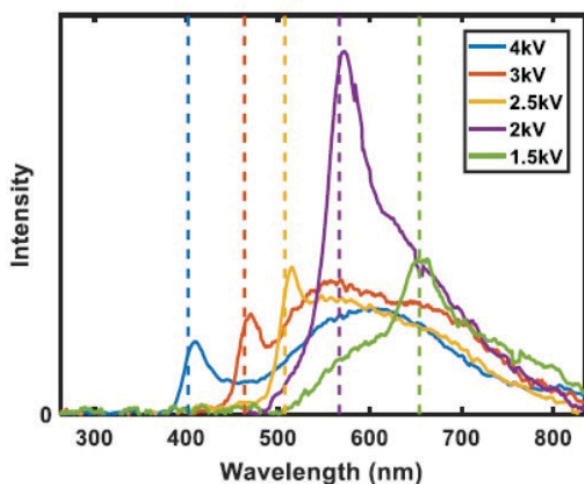
▲ Figure 2: Smith-Purcell radiation spectra from a 50-nm-pitch grating. Different line colors correspond to different kinetic energies of the electron beam. Vertical dashed lines indicate theoretical Smith-Purcell radiation wavelengths.

FURTHER READING

- I. Kaminer, S. E. Kooi, R. Shiloh, B. Zhen, Y. Shen, J. J. López, R. Remez, S. A. Skirlo, Y. Yang, J. D. Joannopoulos, A. Arie, and M. Soljačić, "Spectrally and Spatially Resolved Smith-Purcell Radiation in Plasmonic Crystals with Short-range Disorder," *Physical Review X*, vol. 7, p. 011003, 2017.
- A. Massuda, C. Roques-Carmes, Y. Yang, S. E. Kooi, Y. Yang, C. Murdia, K. K. Berggren, I. Kaminer, and M. Soljačić, "Smith-Purcell Radiation from Low-energy Electrons," *arXiv preprint* arXiv: 1710.05358, 2017.
- S. J. Smith and E. M. Purcell, "Visible Light from Localized Surface Charge Moving across a Grating," *Physical Review*, vol. 92, p. 1069, 1953.

A Scheme for Low-dose Imaging via Conditional Sample Re-illumination

A. Agarwal, V. Goyal, K. K. Berggren
Sponsorship: Gordon and Betty Moore Foundation

Recently, several electron-beam-based low-damage imaging schemes for radiation-sensitive samples (such as proteins and biomolecules) have been investigated. It is now possible to incorporate a Mach-Zehnder interferometer (MZI) in a standard transmission electron microscope (TEM) to perform Elitzur-Vaidman Interaction-free imaging (IFI). We are theoretically investigating the performance of an MZI-based IFI with a Poisson source. We combined IFI with a conditional re-illumination scheme that reduced the probability of imaging errors at low illumination doses.

As a first step, we considered imaging of purely black-and-white pixels. As shown in figure 1, we considered two schemes: classical and IFI, with various imaging detectors. We quantified error as the probability of incorrectly inferring the transparency of a pixel (P_{err}), and damage as the mean number of electrons that scatter off a black pixel (n_{damage}), respectively. At the start of our calculations, we assumed a prior probability q of a given pixel being black. Then, we found expressions to update q based on the electron detection statistics, assuming a Poisson beam with mean λt. If the value of q was within a predefined minimum acceptable error threshold ϵ, we made an inference on whether the pixel was black or white. If this condition was not met, we re-updated q using a second round of detection statistics. This process was repeated a maximum of N_{max} times.

Figure 2 shows the results of imaging utilizing conditional re-illumination, for both classical and IFI. These results were calculated with $N_{max}=1$ (circles with dotted line) and $N_{max}=50$ (crosses with dashed lines) illuminations. For both schemes, conditional re-illumination offered a reduction in n_{damage} at 50 illuminations as compared to single-stage illumination. For classical imaging, N_{damage} was reduced to 1, and for IFI, n_{damage} saturated to 0.67, at $N_{max}=50$.

We are now working on extending these calculations to semi-transparent samples, as well as implementing this illumination scheme in a scanning TEM.

▲ Figure 1: Classical (top) and IFI (bottom) schemes. Blue arrows indicate the possible paths that an incident electron can take. 1, 2, and 3 are imaging detectors – 1 and 2 for transmitted, and 3 for scattered electrons.
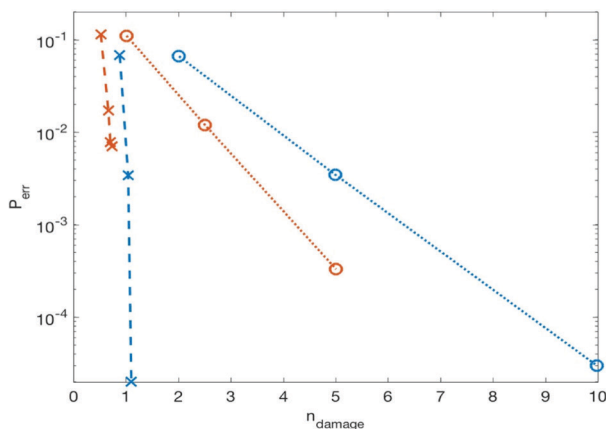
▲ Figure 2: P_{err} vs. n_{damage} for classical (blue) IFI (red) with $\epsilon =0.05$ and q=0.5. Dotted lines with circles indicate values for single-stage illumination, and dashed lines with crosses indicate values for 50 illuminations.

FURTHER READING

- A. Agarwal, C.S. Kim, D. van Dyck, K.K. Berggren, "A Nanofabricated, Monolithic, Path-Separated Electron Interferometer," *Sci. Rep.,* vol. 7, no. 1, 2017.
- R.M. Glaeser, "How Good Can Cryo-EM Become?" *Nat Methods,* vol. 13, no. 1, pp. 28–32, 2016.
- A.C. Elitzur and L. Vaidman, "Quantum Mechanical Interaction-free Measurements," *Foundations of Physics,* vol. 23, no. 7, pp. 987–997, 1993.

A Nanofabricated, Path-separated, Grating Electron Interferometer

A. Agarwal, C.-S. Kim, R. Hobbs, D. van Dyck, K. K. Berggren
Sponsorship: Gordon and Betty Moore Foundation

Recent progress in focused-ion-beam (FIB) technology has enabled the fabrication of electron optical elements such as zone-area plates, phase plates, and beamsplitters. These nanofabricated elements can be used to perform Zernike phase-contrast imaging, holography and beam aberration correction in a conventional transmission electron microscope (TEM). We have fabricated a grating-Mach-Zehnder-electron-interferometer, using FIB milling of a single-crystalline silicon workpiece. As shown schematically in figure 1(a), the interferometer uses two thin layers of silicon as diffraction gratings; the first to split the incident electron beam, and the second to recombine two of the diffracted beams. The gap between the gratings in our interferometer was 20 µm. Fabrication of the gratings from a single crystalline silicon workpiece ensures alignment and precise positioning. We obtained a rotational alignment of ~100 µrad and a grating positioning accuracy of 100 nm. Figure 1(b) is a scanning electron micrograph of this interferometer.

We inserted this interferometer in the sample holder of a 200 kV TEM (JEOL 2010F). We used an electron beam with a diameter of 240 nm on the first grating and convergence semi-angle of 4 mrad in our experiment. As shown in figure 2(b), when imaging the second grating (figure 2(a), sample z-height z_1) at high-resolution (Ψ_0), we obtained a lattice-resolved image of silicon. As we raised our sample holder z-height to move the imaging plane below the second grating (z_2-z_5), the first-order diffracted beam from this grating (Ψ_{0g}) moved closer to the first-order diffracted beam from the first grating (Ψ_{gg}), and the two beams overlapped 20 µm below the second grating (z_6). Figure 2(c) is a high-resolution image of the overlapping beams, showing interference fringes of period 0.32 nm, which was expected from the interference of first-order silicon diffracted beams.

This interferometer could be used to perform electron holography in any TEM, as well as interaction-free imaging using the Elitzur-Vaidman scheme.

▲ Figure 1: Grating interferometer. (a) Schematic of the interferometer. The two diffracted beams Ψ_{0g} and Ψ_{gg} overlap in the 'interference plane". (b) Scanning electron micrograph of the grating interferometer. Each grating had a mean thickness of 45nm, and the gap between the gratings was 20µm.
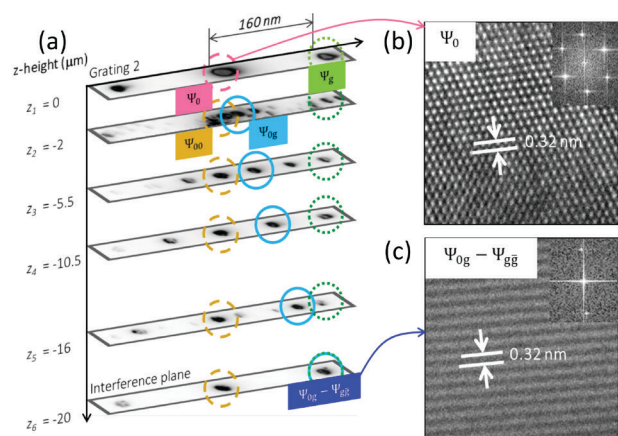
▲ Figure 2: Interferometry in TEM. (a) Diffracted beams imaged at different planes (z_1-z_6) below the second grating. The beams Ψ_{0g} and Ψ_{gg} overlap 20µm below the second grating. (b) High-resolution TEM image of the central beam (Ψ_0) showing the silicon lattice. (c) High-resolution TEM image of the overlap spot in the interference plane, showing interference fringes.

FURTHER READING

- A. Agarwal, C.-S. Kim, R. Hobbs, D. Van Dyck, and K. K. Berggren, "A Nanofabricated, Monolithic, Path-separated Electron Interferometer," *Scientific Reports,* vol. 7(1), pp. 1–10, 2017.
- A. C. Elitzur and L. Vaidman, "Quantum Mechanical Interaction-free Measurements," *Foundations of Physics,* vol. 23(7), pp. 987–997, 1993.
- L. Marton, J. A. Simpson, and J. A. Suddeth, "Electron Beam Interferometer," *Phys. Rev.* vol. 90, p. 490, 1953.

Experimental Characterization and Modeling of Templated Solid-state Dewetting of Thin Single-crystal Films

Y. A. Shin, M. A. L'Etoile, W. C. Carter, C. V. Thompson
Sponsorship: NSF

Solid-state dewetting is a physical phenomenon that disintegrates a continuous film into islands when the film is heated above a characteristic dewetting temperature but kept well below its melting temperature. It is driven by surface energy minimization and mediated via surface diffusion of atoms. Solid-state dewetting has been thought of as an issue in microelectronics, however, it has also demonstrated its potential as a simple patterning method that can be used to generate a complex and regular array of micro- and nano-sized structures in a highly reproducible way [Figure 1a, reference 1]. It starts either from edges of the film or in the continuous flat region by forming a natural hole. Various instabilities that develop at retracting edges have been understood via modeling and experimenting over the past years, including "pinch-off," "corner instability [reference 2]," and "Rayleigh-like instability'[reference 3]." The fingering instability as shown in Figure 1b, which is another instability that creates wire-like structures at retracting edges, is our current focus.

Through experiments, we have found conditions that lead to the fingering instability and have learned that spacing between fingers can be controlled via templating of film edge. We have also found that controlling the period of the fingering process affects the kinetics of the fingering, and we have developed an analytical model that predicts a relationship between the retraction rate and finger period. This model agrees well with experimental results. Our increased understanding of the various instabilities at retracting edges can be used to design templates that will lead to specific complex structures during solid-state dewetting.

However, before we can fully exploit our understanding of templated solid-state dewetting to make designed structures, we must understand natural hole formation in thin films. In polycrystalline films, grain boundary triple junctions facilitate hole formation in a well-understood way, but the formation of holes in single-crystal films (Figure 2) is not well understood. Studying this phenomenon is critical because holes create new edges from which the film retracts. Furthermore, thinner single-crystal films develop more natural holes per unit area, and the growth of these holes can come to dominate the overall reduction of film surface area. Unsuppressed natural hole formation interrupts edge retraction modes that were intentionally patterned to create a specific structure. If controlled, however, the formation of holes could be used to pattern periodic nanostructures that span large length scales, up to several centimeters. In parallel with studying the fingering instability, we are currently working with both Ni films on MgO substrates and Ru films on sapphire substrates to identify and understand the causes of natural hole formation in single-crystal films. By understanding these mechanisms, we aim to develop templated solid-state dewetting into a powerful and cost-effective method for producing nanostructures.
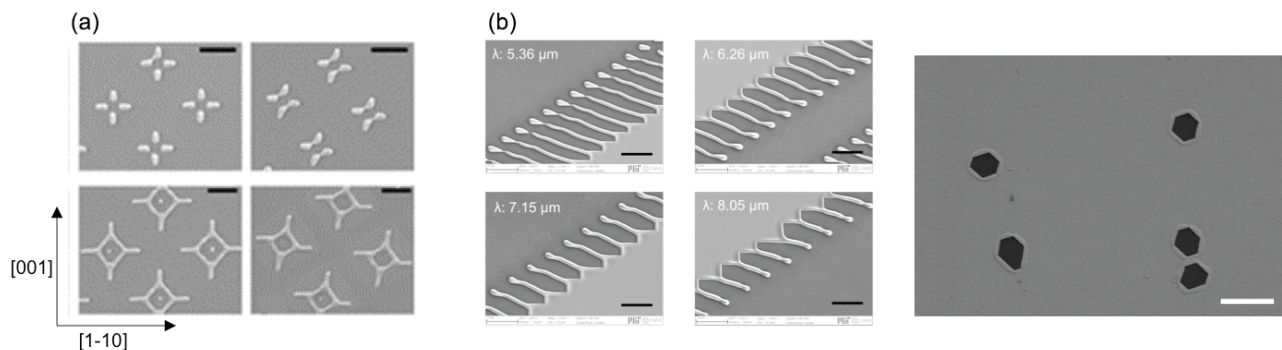
▲ Figure 1: (a) Patterns formed by solid-state dewetting of square patches of Ni films patterned with different sizes and crystallographic orientations. Scale: 10 μm, (b) Wires formed by templating a fingering instability using patterned periodic edge roughness. Scale: 10 μm.

▲ Figure 2: Natural holes in 5 nm thick Ru film on sapphire. Scale 2 μm.

FURTHER READING

- R. V. Zucker, G. H. Kim, J. Ye, W. C. Carter, and C. V. Thompson, "The Mechanism of Corner Instabilities in Single-crystal Thin Films during Dewetting," *J. Appl. Phys.*, vol. 119, pp. 125306, 2016.
- G. H. Kim, W. Ma, B. Yildiz, and C. V. Thompson, "Effect of Annealing Ambient on Anisotropic Retraction of Film Edges during Solid-state Dewetting of Thin Single-crystal Films," *J. Appl. Phys.* vol. 120, pp. 075306, 2016.
- C. V. Thompson, "Solid-state Dewetting of Thin Films," *Annual Review of Materials Research*, vol. 42, pp. 399-434, 2012.